JOURNAL OF AIRCRAFT
Vol. 45, No. 3, May–June 2008

Unsteady Wing–Pylon–Nacelle Interference in Transonic Flow

G. Dietz,* H. Mai,† A. Schröder,‡ and C. Klein§
DLR, German Aerospace Center, 37073 Göttingen, Germany
and
N. Moreaux¶ and P. Leconte**
ONERA, 92322 Châtillon Cedex, France

DOI: 10.2514/1.31363

The interference effects between an unswept supercritical airfoil model and an annular wing representing an engine nacelle were investigated. The investigation aims to better understand and predict the impact of the interference effects on the aeroelastic stability of large modern transport aircraft at transonic speeds. The main objective was to identify potential aerodynamic instabilities in the interference region due to unsteady shock-wave/boundary-layer interactions. The applied model allows the nacelle to roll and yaw relative to the model wing and to pitch the entire model. The aerodynamic response to these movements affects the aeroelastic stability of an aircraft and was also investigated here. The overlap between the wing and the nacelle and the height of the pylon was designed by numerical simulations such that locally supersonic velocities and flow separation in the interference region might occur. Two linear hydraulic jacks inside the model were used to perform prescribed yaw and roll movements of the nacelle, including the pylon. The experiments were conducted up to Mach numbers of 0.84 in an adaptive solid-wall wind tunnel using a hydraulically driven pitch-oscillation setup. Boundary-layer transition was tripped on the wing as well as on the nacelle. The unsteady tests revealed a strong dependency of the aerodynamic response to the structural movement on the topology of the time-averaged flowfield. During the static tests, an aerodynamic instability was detected for certain Mach-number/model-incidence combinations. In addition to the initial objectives, a simple countermeasure was applied in the interference region and its effectiveness was demonstrated.

Nomenclature

c^*	=	reference chord, m
c_d	=	drag coefficient
c_l	=	lift coefficient
c_p	=	pressure coefficient
f^*	=	frequency, Hz
$\mathrm{Im}(v)$	=	imaginary part of complex quantity v
k	=	reduced circular frequency based on c^*
M	=	Mach number
Re	=	Reynolds number based on c^*
$\mathrm{Re}(v)$	=	real part of complex quantity v
Su	=	Sutherland constant, 110.4 K/T^*
T	=	temperature, K
$\mathbf{v}$	=	v_∞^*-normalized local flow velocity vector
x, y, z	=	c^*-normalized Cartesian coordinates
α	=	angle of attack, deg
β	=	nacelle yaw angle, deg
γ	=	nacelle roll angle, deg
δ	=	Lehr's damping coefficient
∇	=	nabla operator

Subscripts

crit	=	critical value
α	=	derivative with respect to model incidence α
β	=	derivative with respect to nacelle yaw angle β
γ	=	derivative with respect to nacelle roll angle γ
0	=	stagnation
∞	=	freestream

Superscripts

$\bar{v}$	=	time-averaged value of v
$\hat{v}$	=	harmonic oscillation amplitude of v
$*$	=	dimensional quantity

Presented as Paper 2018 at the 48th AIAA/ASME/ASCE/AHS/ASC Structures, Structural Dynamics, and Materials Conference, Honolulu, HI, 23–26 April 2007; received 2 April 2007; revision received 4 January 2008; accepted for publication 8 January 2008.

*Head, Aeroelastic Experiments, Institute of Aeroelasticity; currently Managing Director, European Transonic Windtunnel, GmbH; GD@etw.de.
†Research Scientist, Institute of Aeroelasticity; Holger.Mai@dlr.de.
‡Research Scientist, Institute of Aerodynamics and Flow Technology; Andreas.Schroeder@dlr.de.
§Research Scientist, Institute of Aerodynamics and Flow Technology; Christian.Klein@dlr.de.
¶Research and Test Engineer, Department Structural Dynamics and Coupled Systems; Nathalie.Moreaux@onera.fr.
**Research and Test Engineer, Department Structural Dynamics and Coupled Systems; Philippe.Leconte@onera.fr.

I. Introduction

A JOINT aeroelastic research project called WIONA (wing with oscillating nacelle) was performed by the ONERA French aerospace lab and the DLR, German Aerospace Center. This project concentrates on the aerodynamic interference associated with the wing, pylon, and high-bypass-ratio fanjet engines installed on a typical transport aircraft at transonic speeds. The project aims to understand observed unsteady aeroelastic phenomena to ensure its accurate prediction and to derive design criteria, as well as countermeasures, to avoid aeroelastic instabilities. An experimental wind-tunnel investigation was conducted within the research project WIONA. The present paper describes its experimental setup using an unswept supercritical airfoil model and an annular wing representing an engine nacelle, the test results at sub- and transonic flow conditions, and the test-data interpretation.

In the past, the bypass ratio of transport-aircraft fanjet engines was increased to about 6–9 for improving jet-engine efficiency [1,2]. Future developments aim to reach bypass ratios up to 15–20, but might be limited by installation space [3]. Ducts are used, for

example, to reduce noise emission. The resulting large-diameter engines and their typical underwing nacelle installations influence the aircraft substantially: safety, structural weight, drag, maximum lift, propulsion efficiency, control, maintainability, and aeroelastic stability are affected. Engine–airframe integration (particularly, the definition of the nacelle locations) constitutes a multi-objective optimization problem with several constraints such as ground clearance or yaw moment after engine failure. However, the wing–nacelle overlap, the wing–nacelle distance, and the pylon geometry determine the wing–pylon–nacelle interference; high local velocities may occur, which can cause high-interference aerodynamic drag. Even local supersonic regions terminated by shock waves may be found in the interference region, which strongly affect the aeroelastically relevant unsteady airloads [4–6]. In such cases, unforeseen flight-envelope-limiting interference such as aerodynamic instabilities may occur due to inappropriate design of the wing–pylon–nacelle region, either close to cruise or, more likely, close to dive conditions.

The present study reports results from experiments on such interference effects between an unswept supercritical airfoil model and an annular wing representing a long-duct engine nacelle with tripped boundary-layer transition at sub- and transonic flow conditions. The main objective is to identify possible aerodynamic instabilities in the interference region due to unsteady shock-wave/boundary-layer-separation interactions. The elastic structure of a real wing–pylon–nacelle configuration allows particular yawing and rolling of the nacelle relative to the wing and pitching of the wing–pylon–nacelle combination. Therefore, the test setup is designed to roll and yaw the nacelle relative to the wing and to pitch the entire model. The aerodynamic response to these movements is investigated here. The movements of the model and its components are measured by accelerometers and optical position detection. The aerodynamic loads are measured by pressure sensors and a piezoelectric balance. Furthermore, the steady pressure distributions on the pylon are measured by pressure-sensitive paint (PSP), and instantaneous flow velocity distributions in one plane in the interference region are measured by particle-image velocimetry (PIV). The evaluation of the experimental results contributes to the understanding of both the dependency of the aerodynamic response to the structural movement on the topology of the time-averaged flowfield and the possible aerodynamic instabilities in the interference region.

II. Setup

The present investigation was carried out in the 1×1 m adaptive test section of the German–Dutch Wind Tunnels foundation's Transonic Wind Tunnel, Göttingen (DNW-TWG), a continuously working facility, using a complex model that was mounted in a forced-pitch-oscillation setup.

A. Transonic Adaptive Solid-Wall Wind Tunnel

The ratio of the wind-tunnel height to the reference wing chord of the investigated WIONA model is 2.78. Solid wind-tunnel walls are applied to provide well-defined boundary conditions for in-tunnel numerical simulations. However, wall adaptation is used to avoid wind-tunnel blockage and to avoid strong wind-tunnel interference effects that would complicate the test-data interpretation. For each test point, the top and bottom walls of the test section are adapted to the steady flow around the model at the mean angle of attack. The wall adaptation is based on static pressure measurements in the midsection of the wind-tunnel test-section top and bottom walls. The accuracy of the wall pressures is estimated to be 0.35% with respect to the test stagnation pressure. The wall interference is minimized by a one-step method of wall adaptation based on a Cauchy-type integral [7]. The displacement thickness of the turbulent wind-tunnel-wall boundary layer is predicted by Head's method [8] and is added to the wall shapes; top- and bottom-wall displacement thicknesses are obtained according to the measured pressure gradients at each wall, whereas the gradient is neglected for the sidewalls.[††] This adaptation to the mean steady position of the model yields nearly minimum residual wall interference for moderately oscillating airfoil models.[††]

However, in the present case, 2-D wall adaptation is applied to an inherently 3-D flow. The annular wing in the midsection of the model induces a displacement and rotation, which affects the midsection wind-tunnel-wall pressure distribution. So this local installation governs the wall adaptation. Thus, the applied wall shapes yield minimum residual wall interference in the midsection. Next to the midsection (particularly, beside the nacelle), the walls are overadapted such that the stream tube has a larger cross section than with an adaptation to a corresponding clean airfoil model. Thus, the model side-section pressure distributions cannot be directly compared with simulations assuming free-flight far-field boundary conditions. For comparison with computations, it is recommended to numerically simulate the entire model as well as the wind-tunnel walls using the measured wall shapes.

The lowest value for the wind-tunnel resonance frequency can be estimated using the method described by Voß [9]. Based on this method, the ratio of model excitation to wind-tunnel resonance frequency is lower than 51% for the reported data.

B. Forced-Pitch-Oscillation Setup

The model is mounted to a hydraulically driven pitch-oscillation test setup that is arranged symmetrically outside of the wind-tunnel test-section sidewalls. The angle of attack of the symmetrically installed model can be varied by ± 20 deg via two hydraulic exciters operated in phase opposition. Forced pitch oscillations up to a dimensional frequency of 60 Hz are possible. The suspension system comprises a compensator, a bearing, a piezoelectric balance, and a bar acting as a reference for laser triangulators. Using these, the instantaneous angle of attack is measured by triangulation. The setup allows the adjustment and measurement of the angle of attack α with an accuracy of ± 0.02 deg. During the present tests, forced harmonic pitch excitation at amplitudes up to $\hat{\alpha} = 0.8$ deg for a reduced frequency of $k = 0.1$ and amplitudes of $\hat{\alpha} = 0.2$ deg for reduced frequencies up to $k = 0.4$ are performed.

C. WIONA Wind-Tunnel Model

The WIONA wind-tunnel model was designed to exhibit aerodynamic interference as it may occur due to inappropriate design of the wing–pylon–nacelle region of modern civil aircraft, either close to cruise or, more likely, close to dive conditions. However, a generic shape was chosen to reduce complexity as much as possible and to enable a detailed physical interpretation of the observed phenomena. One main design objective of the generic model was to obtain a reasonably strong shock wave in the interference region to enable potential aerodynamic instabilities due to unsteady shock-wave/boundary-layer-separation interactions. Figure 1 shows the model mounted in the adaptive test section of the DNW-TWG wind tunnel.

Laminar-turbulent boundary-layer transition is tripped at 7.5% local chord on the wing, as well as on the nacelle, by disks with a height of 0.046%, a diameter of 0.278%, and a separating distance of 0.706% wing chord length. The effectiveness of the transition tripping is checked by infrared imaging in former experiments with a similar setup at similar flow conditions. The tripping is applied in an attempt to obtain a better comparison with numerical simulations, because an accurate prediction of the transition region is still an unsolved problem (particularly for unsteady flows).

Preliminary flow simulations are carried out to define the final model geometry. Geometric characteristics of the model configuration (namely, the wing sweep), the overlap between wing and nacelle, and the height of the pylon are varied systematically. These design simulations showed that the strength of a shock wave in the interference region strongly depends on the nacelle–pylon yaw angle and the wing–nacelle overlap, whereas the wing-sweep angle has a weak impact [6]. Therefore, the WIONA model consists of an

[††]Private communication with M. Jacobs, March 2007.

Fig. 1 Photograph of the WIONA model mounted in the adaptive test section of the DNW-TWG wind tunnel.

unswept rectangular wing with an annular wing as a generic engine nacelle mounted beneath a rigid pylon. The wing shape is based on the airfoil VC-Opt [10], which has a 9.2% relative thickness. It has a 1-m span and a chord length of $c^* = 0.36$ m, which is used for reference. The nacelle airfoil exhibits a 7.0% relative thickness. Its shape and the pylon shape are described by Soda and Tefy [11] and are based on the DLR-F6 geometry [12]. The nacelle's outer diameter is 0.144 m and it has a length of 0.243 m. The nacelle's axis has an incidence of -0.6 deg relative to the wing chord, which defines the model incidence. The wing–nacelle overlap is 25% wing chord; the smallest chord-normal distance between the wing pressure side and the nacelle outside amounts to 2.8% wing chord. The pylon is uncambered, its leading edge intersects the wing leading edge, and it has a thickness of 8.1% wing chord.

The model performed prescribed yawing $\hat{\beta} \leq 0.5$ deg and rolling $\hat{\phi} \leq 5$ deg motions of the nacelle–pylon entity relative to the wing, either isolated or combined. Two linear hydraulic jacks located inside the wing body are used to move the nacelle–pylon entity. A flexible metallic coupling device, stiff enough to carry the nacelle loads, was designed using numerical simulation. Figure 2 shows a schematic view of the excitation system.

The available performance of the forced-pitch-oscillation setup and of the model's inner excitation system required the model and the nacelle inertia moments to be limited. The design of the model is carried out while taking constant care to keep its overall mass as low as possible; to keep its mass distribution with respect to the pitching, rolling, and yawing axes in balance; and to enable the implementation of a comprehensive instrumentation. The wing body and the pylon are manufactured from aluminum alloy. Most parts of the excitation system are made from high-tensile steel. The nacelle itself is set up as a foam–polyurethane–wood compound. The final design of the WIONA model is calculated both for static and dynamic loads using the load distributions provided by the preceding preliminary design simulations.

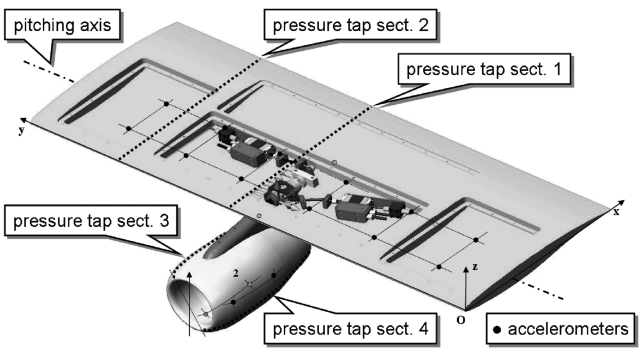

Fig. 2 Sketch of the WIONA model showing its inner excitation system and the location of the pressure-tap sections.

The wing-pylon sealing deserved closer attention. The required rolling and yawing of the nacelle–pylon entity relative to the wing come with significant gaps, which have to be sealed. A pretest revealed that insufficient sealing might significantly reduce the strength of the shock wave in the interference region. Thus, a special rubber sealing between the pylon and the wing is designed and thoroughly tested.

D. Measuring Techniques

To generate an experimental database for the validation of advanced numerical simulation codes, different measuring techniques are synchronized and applied simultaneously.

1. *Transducers*

The wing of the WIONA model (see Fig. 2) is equipped with 110 differential pressure transducers (Kulite XCQ-093-5D) and one absolute pressure transducer (Kulite LQ24-080-25A), which are arranged in two streamwise sections at 52.75% (section 1 in Fig. 2) and 79.5% span (section 2). The nacelle is equipped with 36 absolute pressure transducers: 27 Kulite XCQ-062-25A and 9 Kulite LL-072-25A. These are arranged in two streamwise sections at nacelle-axis angles of -26 deg (section 3) and 154 deg (section 4), respectively; therefore, one pressure-tap section in the wing and one nacelle section are located in the wing–pylon–nacelle interference region. Both of the other sections may be used as undisturbed reference. The local pressure-based lift, pitching-moment, and drag coefficients are integrated from the measured model surface-pressure data. The accuracy of the measured pressures at the model surface is estimated to be 0.5% with respect to the test stagnation pressure.

Additionally, the model is equipped with 18 piezoelectric miniature accelerometers (Endevco 25A and 2250A). Twelve accelerometers are mounted in six streamwise sections of the wing (four in the nacelle and two in the pylon) to measure the model's instantaneous movements and its possible elastic deformation. Figure 2 indicates the location of the pressure-tap sections and the accelerometers.

Inside the model, each of the two linear hydraulic jacks is closed-loop controlled using one linear inductive position sensor. A potentiometer and a Hall sensor are linked to the flexible metallic coupling device to measure the roll and the yaw angle of the nacelle, respectively.

Outside of the wind-tunnel walls, the WIONA model is mounted in the pitch-oscillation setup on each side via a piezoelectric balance of high stiffness [13] to measure the steady and unsteady global lift and pitching moment. Unfortunately, the rather stiff hydraulic lines for driving the nacelle motion had to be led across the balance and therefore affect the balance-data quality. In particular, the reliability of the balance drag data is only limited. Two laser triangulators on each side of the wind tunnel measure the instantaneous pitch of the model.

2. *Particle-Image Velocimetry*

A PIV system [14] is used to obtain information on the velocity distribution in the interference region. The PIV system consists of one camera facing the spanwise direction through an observation window around the model-pitching axis in the wind-tunnel sidewall. The laser light sheet is created by a double-pulse Nd:YAG laser with the energy of 300 mJ per pulse. The light sheet is perpendicular to the pitching axis and located at 52.5% model span, close to the pressure-tap sections in the interference region. Thirty-two PIV samples are recorded for almost every single test-data point at which unsteady data such as pressures, global forces, model position, and motion data are measured. This recording is time-synchronized to the sampling of the other data. Because of the laser's maximum double-pulse frequency of 10 Hz, only a few PIV recordings per model oscillation cycle could be taken within a short time series, depending on the model frequency. With different samples from different cycles, it is possible to twice get 16 samples that are equally spaced with respect to the phase of the model oscillation. Every PIV

Table 1 Modal parameters of the WIONA model mounted in DNW-TWG up to 400 Hz [16]

No.	Mode description	f^*, Hz	δ, %	Mode indicator function
1	First wing bending	56.3	1.61	990
2	First nacelle yaw	64.9	7.63	981
3	First nacelle pitch	74.3	2.18	964
4	First wing torsion symmetry	124.7	2.20	993
5	Second wing bending	147.1	1.51	991
6	Second nacelle yaw	160.6	4.05	987
7	First wing torsion anti.	198.2	2.06	925
8	Third wing bending	233.0	3.78	901
9	Wing torsion and nacelle ovalization	277.6	1.52	957
10	First nacelle ovalization	316.4	4.88	966
11	Second nacelle ovalization	349.5	2.48	990
12	Second pylon bending	377.1	2.69	995
13	Second wing torsion	390.2	0.87	801

recording yields about 3450 valid velocimetry vectors, which are each evaluated from a 2×2 mm^2 area.

3. Pressure-Sensitive Paint

A PSP system [15] is used for optically measuring static pressure distributions on the WIONA model pylon. Thus, the pylon is coated with paint in three consecutive layers: screen layer, contact layer, and active layer. The screen layer is a white paint that creates an optical uniformity on the model surface. The contact layer ensures adhesion between the screen and the active layer. The active layer consists mainly of three components: a binding polymer layer that is highly permeable to oxygen, a pressure-sensitive luminescent luminophore, and intensity-sensitive luminophores for correction of the non-homogeneous illumination distribution. Six markers are applied to the rigid-but-moving pylon surface to match the camera pictures and for spatial reconstruction of the pressure distributions.

A xenon UV-light source illuminated the model in the test section using fiber optics. Two 12-bit-resolution CCD cameras with optical filters for the pressure (blue, 450–550 nm) and the reference (red, 600–650 nm) images are used for data acquisition. Minimum exposure times amount at about 10 s for a typical distance of 0.5 m between the cameras and the model.

The optical pressure sensor on the model pylon is quantitatively calibrated in the wind tunnel by changing the tunnel's total pressure at constant temperature in still air. An in situ calibration for the evaluation of the pressure distributions is added. It is determined by comparison of selected pressure-tap values with the PSP results at the location of the corresponding pressure taps in the wind-tunnel model. One PT100 temperature sensor is used to measure the pylon surface temperature to correct the pressure evaluations.

III. Results and Discussion

A dynamic characterization of the WIONA model is performed once the model is installed in the wind tunnel. Table 1 collects the identified modal parameters up to a frequency of 400 Hz. These data confirmed the results of dynamic finite element method analysis during the model design phase.

The following wind-tunnel test results are extracted from more than 1100 time series of data and 31,000 PIV recordings, which are acquired during 11 days of testing. Data for static model conditions are recorded for various sub- and supercritical Mach numbers M_∞ of 0.5, 0.7, 0.755, 0.775, 0.8, 0.82, and 0.84 and at angles of attack α of -0.6 to 1.2 deg in 0.1-deg increments. At the same Mach numbers, forced-oscillation data are acquired for model pitching, nacelle yawing, nacelle rolling, model pitching plus nacelle yawing, and model pitching plus nacelle rolling for time-averaged incidences $\bar{\alpha}$ of -0.4, 0, and 1.0 deg. During the static tests, an aerodynamic instability was detected for certain Mach-number/incidence combinations. Such an instability may be the unforeseen result of an inappropriate shaping of the wing–pylon–nacelle region. If detected in a late design status of a new aircraft, costly reshaping of the interference region might be necessary. As an alternative, a simple countermeasure is proposed. A prototype is applied in the interference region and its effectiveness is demonstrated.

Figure 3 shows measured time-averaged pressure distributions in the interference section on the nacelle ($-0.425 \leq x \leq 0.25$, lower plot) and on the wing ($0 \leq x \leq 1$, upper plot). Present test data are compared with pretest results. During the pretest, the wing-pylon gap is sealed by a brush. The present test data indicate a strong wing–pylon–nacelle interference by a local supersonic region ($3\% \leq x \leq 15\%$), which is terminated by a shock wave. In contrast, the pretest pressure distributions and PSP data (Fig. 3, middle) at the same flow conditions reveal only a small supersonic region with almost isentropic recompression. Apparently, the brush sealing allows a streamwise venting such that the boundary layer starts thickening upstream [17]. This thickening of the boundary layer is expected to provoke the isentropic recompression. Because the project aims to study a strong wing–pylon–nacelle interference, the brush sealing is replaced by a specially designed rubber sealing between the pylon and the wing.

Figure 4 shows measured time-averaged pressure distributions in the wing and nacelle reference sections corresponding to the interference-section data in Fig. 3. Pretest and present test data match very well. The flow at $3\% \leq x \leq 15\%$ is clearly subsonic. A comparison with Fig. 3 emphasizes that the model design is

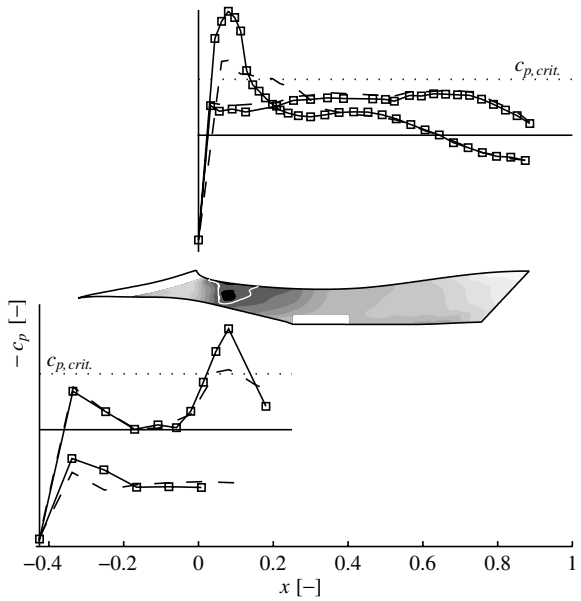

Fig. 3 Measured time-averaged pressure distributions $c_p(x)$ in the interference section; pretest results (dashed line) compared with present test data (squares and solid line); pressure-tap data along the wing (top) and along the nacelle (bottom); pretest PSP results on the pylon for low pressure (dark), high pressure (light) and the sonic line (white); $M_\infty = 0.757 \pm 0.3\%$, $Re_\infty = 2.28 \times 10^6 \pm 0.8\%$, $Su_0 = 0.361 \pm 0.5\%$, $\alpha = 0.01$ deg ± 0.02 deg, $\beta = 0$ deg, and $\gamma = 0$ deg.

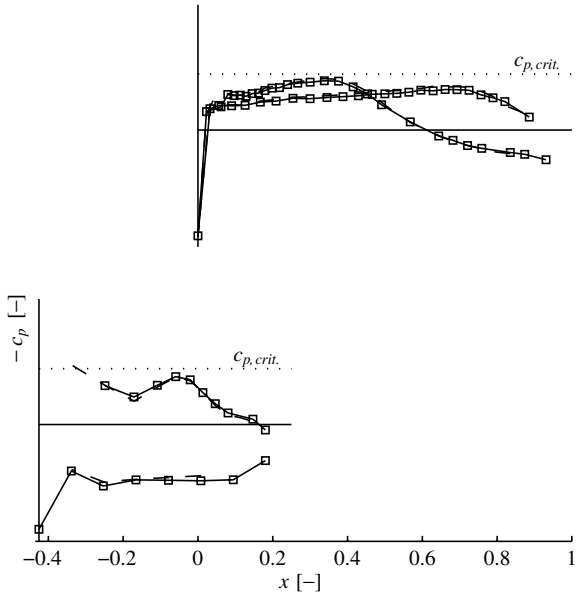

Fig. 4 Measured time-averaged $c_p(x)$ in the reference sections; pretest results (dashed line) are compared with present test data (squares and solid line); pressure-tap data along the wing (top) and along the nacelle (bottom); $M_\infty = 0.757 \pm 0.3\%$, $Re_\infty = 2.28 \times 10^6 \pm 0.8\%$, $Su_0 = 0.361 \pm 0.5\%$, $\alpha = 0.01\,\text{deg} \pm 0.02\,\text{deg}$, $\beta = 0\,\text{deg}$, and $\gamma = 0\,\text{deg}$.

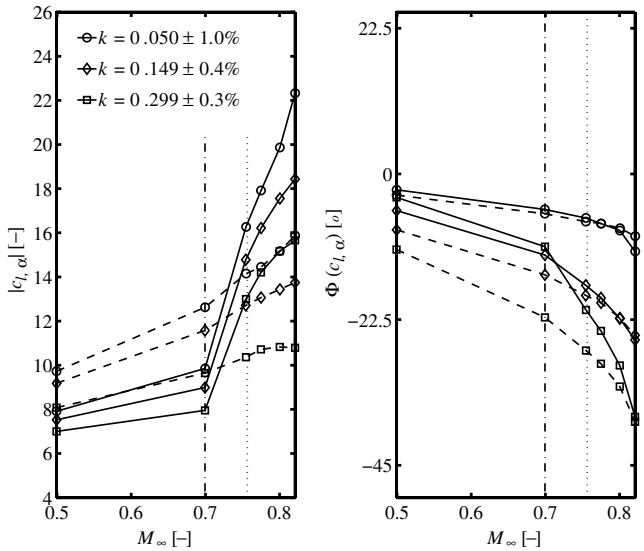

Fig. 5 Magnitude and phase distributions of measured pressure-based lift derivatives $c_{l,\alpha}$ vs M_∞ for forced harmonic pitch oscillations with reduced frequency k; interference section (solid line) compared with reference-section data (dashed line); interference-region sonic (dashed-dotted line) and nacelle-lift divergence (dotted line) are indicated by vertical lines; $Re_\infty = 2.21 \times 10^6 \pm 4.1\%$, $Su_0 = 0.360 \pm 0.5\%$, $\bar{\alpha} = 0.04\,\text{deg} \pm 0.02\,\text{deg}$, $\hat{\alpha} = 0.15\,\text{deg}$, $\beta = 0\,\text{deg}$, and $\gamma = 0\,\text{deg}$.

appropriate to gain the intended strong wing–pylon–nacelle interference.

The pretest also revealed that static nacelle yaw angles of $\beta = +3$ and -3 deg exhibit massive flow separation on the leeward pylon side. This flow topology is out of the scope of the present project objectives. Thus, the present test concentrates on a mean yaw angle of $\beta = 0$ deg. However, selected static and forced-oscillation tests are also performed for a mean yaw angle $\beta = -3$ deg, but are not shown here.

A. Forced-Oscillation Results

The integration of the unsteady pressure distributions for forced harmonic pitch oscillations yields local pressure-based unsteady lift derivatives $c_{l,\alpha}$, which are plotted in Fig. 5 vs Mach number. Interference-section data are compared with the clean airfoil data as a reference. The data from the wing pressure tap (section 2 in Fig. 2) represent the clean airfoil, are integrated, and are used as reference data (see Fig. 2). The interference-section data represent the integral forces in a section immediately beside the pylon, comprising the integrated and added measurements from the pressure tap (sections 1, 3, and 4). Here, the main characteristics of the flowfield are indicated for orientation: the Mach number at which locally supersonic velocities occur in the interference region and the lift-divergence Mach number at which a local nacelle-lift maximum with respect to Mach number occurs at constant model incidence.

Figure 5 compares the magnitude and phase distributions of such lift derivatives $c_{l,\alpha}$ for the interference section with those of the reference section. For a subsonic Mach number of $M_\infty = 0.5$, the magnitude and phase difference of the lift response to the model pitching are measured to be smaller in the interference section than in the reference section. The higher the reduced frequencies of k (0.05, 0.15, and 0.3), the lower the derivative magnitude. The lift-derivative magnitudes $|c_{l,\alpha}|$ increase with a growing Mach number. This slope increases significantly for the interference section when supersonic velocities occur at $M_\infty \geq 0.7$. The phase lag of the lift response to the model-pitch motion $-\Phi(c_{l,\alpha})$ increases with a rising Mach number. At $M_\infty = 0.5$, the phase lag is smaller in the interference section than in the reference section. For a transonic Mach number of $M_\infty = 0.82$, the measured phase lags at all reduced frequencies are about the same in both sections. Previous investigations of the authors [18–20] indicate that these relatively high phase lags combined with the structural washout effect of a flexible rearward swept wing will disproportionately decrease the flutter stability limit with increasing Mach number, compared with a flat-plate flutter boundary.

Figure 6 shows unsteady pressure distributions $\text{Re}(c_{p,\alpha})$ and $\text{Im}(c_{p,\alpha})$ at the nacelle's outer side and the wing pressure side in the interference section. The data are measured on the harmonic pitching model at different oscillation amplitudes $\hat{\alpha}$ of 0.14, 0.30, and 0.61 deg, but at a constant reduced frequency $k = 0.150$ and at a constant supercritical Mach number of $M_\infty = 0.755$. At $x = 13\%$, a pressure peak occurs on the wing pressure side. Its location corresponds to the shock-wave position in Fig. 3. The positive real part $\text{Re}(c_{p,\alpha})$ in Fig. 6 indicates that the shock wave travels upstream with increasing model incidence. The phase lag of the pressure response to the model pitch amounts to $-\Phi[c_{p,\alpha}(x = 13\%)] \approx 22$ deg. Figure 6 demonstrates that these shock-wave dynamics govern the lift derivatives in the interference section at supercritical Mach numbers, which are shown in Fig. 5. Furthermore, the unsteady pressure distributions for pitch-oscillation amplitudes $\hat{\alpha} = 0.14$ and 0.30 deg match almost exactly, whereas the data for $\hat{\alpha} = 0.61$ deg differ. Thus, taking into account the inherently nonlinear steady transonic flowfield, linearization of the unsteady flowfield is appropriate up to pitch-oscillation amplitudes $\hat{\alpha} \leq 0.30$ deg.

Figure 7 compares the magnitude and phase distributions of the local lift derivatives in the interference section due to nacelle-yaw $c_{l,\beta}$ and nacelle-roll $c_{l,\gamma}$ oscillations. The magnitude of the lift response to the nacelle-yaw motion is higher than that with nacelle-roll motion. However, it is an order of magnitude smaller than with the lift derivatives, due to model-pitch oscillation $c_{l,\alpha}$, as shown in Fig. 5. The occurrence of the locally supersonic flow in the interference region strongly affects both magnitude slopes. Nevertheless, the phase difference between the nacelle motion and the lift response does not change much, except for a phase reversal in $c_{l,\gamma}$ at $M_\infty = 0.755$.

Figure 8 clarifies the occurrence of the phase-reversal phenomenon in Fig. 7. The pressure-based lift in the interference section is plotted vs nacelle roll angle γ. Lift hysteresis loops are shown for three Mach numbers ($M_\infty = 0.499$, 0.755, and 0.800), which are obtained by phase-locked averaging the data from 320

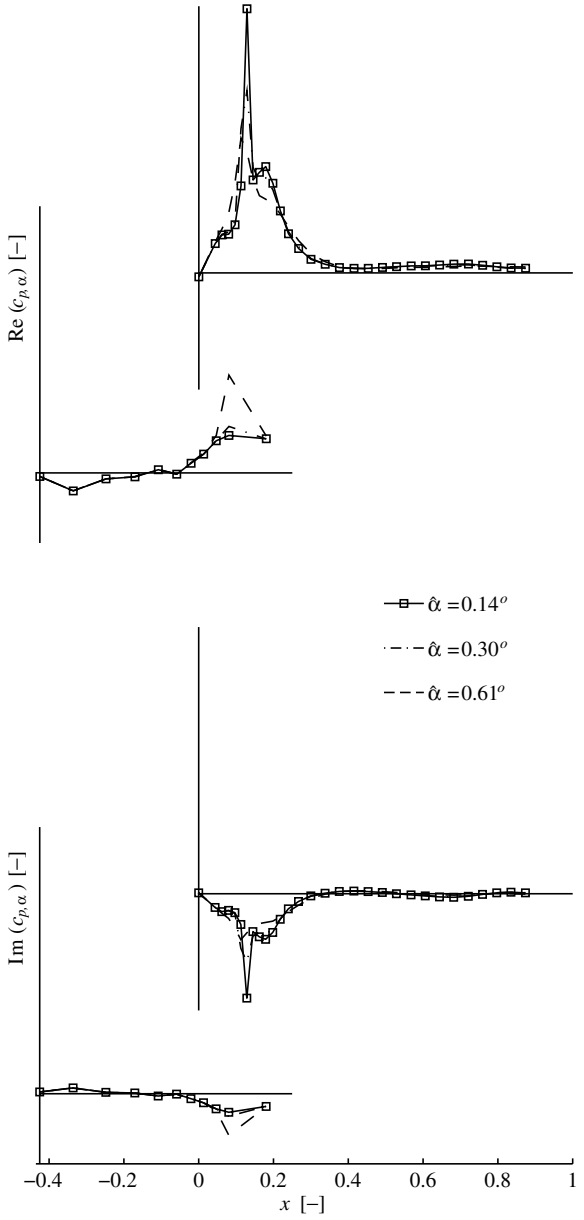

Fig. 6 Unsteady pressure distributions $c_{p,\alpha}$ for forced harmonic pitch oscillations with amplitude $\hat{\alpha}$ at reduced frequency $k = 0.150 \pm 0.1\%$; nacelle outer side and wing pressure side in the interference section are shown; $M_\infty = 0.755 \pm 0.1\%$, $Re_\infty = 2.27 \times 10^6 \pm 0.3\%$, $Su_0 = 0.361 \pm 0.3\%$, $\alpha = 0.03\,\text{deg} \pm 0.02\,\text{deg}$, $\beta = 0\,\text{deg}$, and $\gamma = 0\,\text{deg}$.

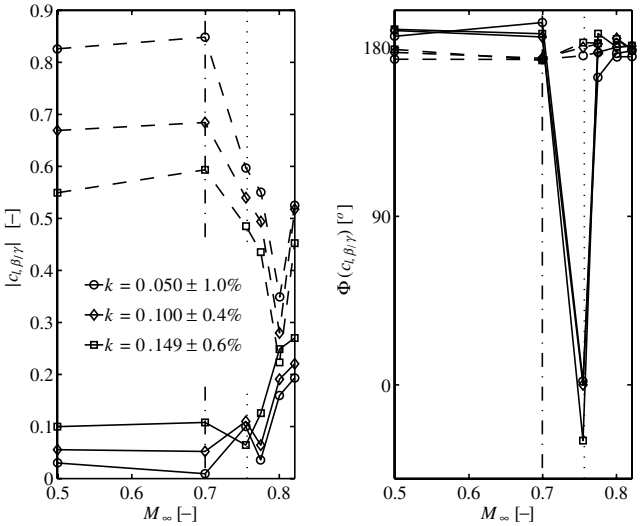

Fig. 7 Magnitude and phase distributions of measured lift derivatives $c_{l,\beta/\gamma}$ vs M_∞ for forced harmonic yaw β (dashed line), and roll γ (solid line) oscillations with reduced frequency k. interference-region sonic (dashed-dotted line), nacelle-lift divergence (dotted line) are indicated by vertical lines; $Re_\infty = 2.21 \times 10^6 \pm 4.6\%$, $Su_0 = 0.360 \pm 0.8\%$, $\alpha = 0.04\,\text{deg} \pm 0.02\,\text{deg}$, $\bar{\beta} = 0\,\text{deg}$, $\hat{\beta} = 0.44\,\text{deg}$, $\bar{\gamma} = 0\,\text{deg}$, and $\hat{\gamma} = 4.66\,\text{deg}$.

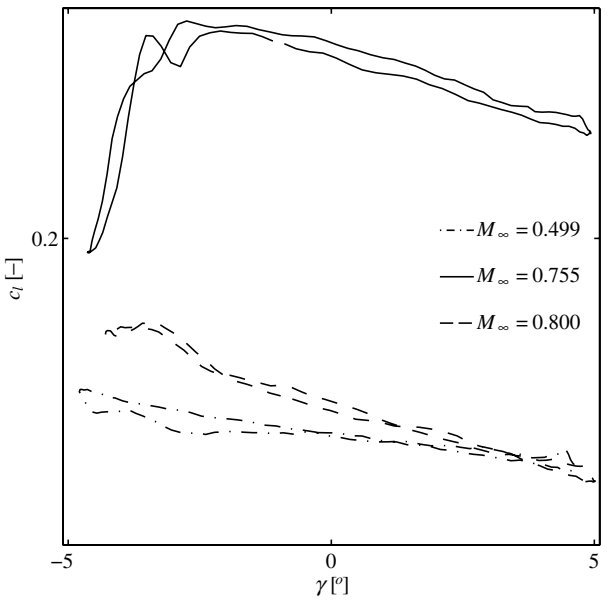

Fig. 8 Pressure-based interference-section lift hysteresis loops for forced harmonic roll γ oscillations with reduced frequency $k = 0.149 \pm 0.2\%$; $Re_\infty = 2.21 \times 10^6 \pm 3.3\%$, $Su_0 = 0.359 \pm 0.4\%$, $\alpha = 0.03\,\text{deg} \pm 0.02\,\text{deg}$, $\beta = 0\,\text{deg}$, $\bar{\gamma} = 0\,\text{deg}$, and $\hat{\gamma} = 4.67\,\text{deg}$.

oscillation periods. The observed hysteresis is within the measurement accuracy for all three Mach numbers and should therefore not be overinterpreted. However, the lift at low roll angles shows a significant break-in for $M_\infty = 0.755$. A deeper analysis of the pressure distributions indicates that this break-in most likely corresponds to flow separation close to the nacelle trailing edge in the interference region (not shown here). The upstroke and downstroke of all hysteresis loops almost match, corresponding to the Fig. 7 observations that show derivative phase differences of $\Phi(c_{l,\gamma}) \approx 0$ and 180 deg, respectively. The derivatives' magnitudes are represented by the absolute values of the averaged hysteresis slopes. Taking into account roll-oscillation amplitudes $\hat{\gamma} \leq 4.67\,\text{deg}$, the averaged slope for $M_\infty = 0.755$ is positive, whereas both other slopes are negative. This corresponds to the phase jump from $\Phi(c_{l,\gamma}) \approx 180$ to 0 deg, and vice versa, with increasing Mach number. Apparently, such a phase reversal would not occur for smaller roll-oscillation amplitudes ($\hat{\gamma} \leq 2.5\,\text{deg}$).

The model lift response to combined nacelle-yaw and model-pitch oscillations at the same reduced frequency $k = 0.149$ is plotted in Fig. 9. Data are compared for several phase angles $\Phi(\beta_\alpha)$ between those two degrees of freedom (DOF). For phase angles $\Phi(\beta_\alpha) \approx \pm 90\,\text{deg}$, the magnitudes $|c_{l,\alpha}|$ essentially match the values of the pure pitch oscillation (see Fig. 5), but the phase angles differ. For phase angles $\Phi(\beta_\alpha) \approx 0$ and 120 deg, the phase angles $\Phi(c_{l,\alpha})$ basically match the values of the pure pitch oscillation (see Fig. 5), but the magnitudes differ. When the Mach number increases above its critical value, the impact of the superposed nacelle-yaw motion decreases up to $M_\infty = 0.8$. Of course, the differences in phase and magnitude compared with the pure pitch oscillation, as it is observed here, depend on the amplitude ratio of the yaw to the pitch motion.

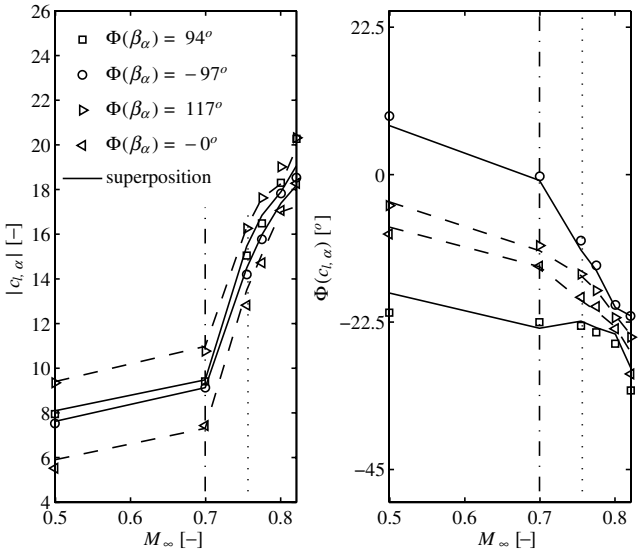

Fig. 9 Magnitude and phase distributions of $c_{l,\alpha}$ vs M_∞ for forced combined yaw β / pitch α oscillations with reduced frequency $k = 0.149 \pm 0.7\%$; directly measured data (symbols) and superposed single-DOF measured data (solid and dashed line); interference-region sonic (dashed-dotted line) and nacelle-lift divergence (dotted line) are indicated by vertical lines; $Re_\infty = 2.21 \times 10^6 \pm 3.8\%$, $Su_0 = 0.359 \pm 0.6\%$, $\alpha = 0.04\,\text{deg} \pm 0.02\,\text{deg}$, $\hat{\alpha} = 0.14\,\text{deg}$, $\bar{\beta} = 0\,\text{deg}$, $\hat{\beta} = 0.44\,\text{deg}$, and $\gamma = 0\,\text{deg}$.

Figure 10 shows the magnitude and phase distributions of the lift derivatives $c_{l,\alpha}$ for combined nacelle-roll and model-pitch oscillations at the identically reduced frequency of $k = 0.149$. The data from combined motion testing are compared with results that are calculated from the data obtained in pure model-pitch and pure nacelle-roll tests. Lines and corresponding symbols match fairly well, except for those at $M_\infty = 0.755$ (see the preceding discussion on phase reversal). Thus, the unsteady flowfield seems to behave essentially linearly with respect to the pitch oscillation $\hat{\alpha} = 0.14\,\text{deg}$ and the roll oscillation $\hat{\gamma} = 4.66\,\text{deg}$ around its steady state, such that linear superposition of the single-DOF data is appropriate. Figure 9 also demonstrates this in a similar manner for a combined pitch $\hat{\alpha} = 0.14\,\text{deg}$ and yaw oscillation $\hat{\beta} = 0.44\,\text{deg}$.

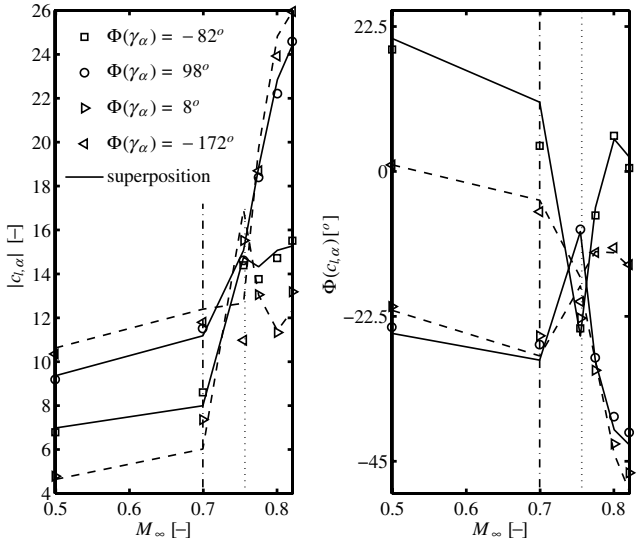

Fig. 10 Magnitude and phase distributions of $c_{l,\alpha}$ vs M_∞ for forced combined roll/pitch (γ/α) oscillations with reduced frequency $k = 0.149 \pm 0.5\%$; directly measured data (symbols) and superposed single-DOF measured data (solid and dashed line); interference-region sonic (dashed-dotted line) and nacelle-lift divergence (dotted line) are indicated by vertical lines; $Re_\infty = 2.21 \times 10^6 \pm 3.8\%$, $Su_0 = 0.360 \pm 0.6\%$, $\alpha = 0.03\,\text{deg} \pm 0.02\,\text{deg}$, $\hat{\alpha} = 0.14\,\text{deg}$, $\beta = 0\,\text{deg}$, $\bar{\gamma} = 0\,\text{deg}$, and $\hat{\gamma} = 4.66\,\text{deg}$.

B. Aerodynamic Instability

It is known that inappropriate high-bypass jet-engine integration may cause aircraft vibrations at certain Mach-number/incidence combinations. The authors assume that an unsteady shock-wave/boundary-layer interaction in the wing–pylon–nacelle interference region provides the unsteady airloads that in turn induce the structural vibrations. Such a mechanism would work in the same way as the well-known transonic shock buffet of airfoils [6,21–23]. Indeed, the present tests revealed such an aerodynamic instability for certain Mach-number/incidence combinations with the model at rest.

Figure 11 shows typical time-averaged pressure distributions in the interference section. The pressure-side wing-surface distribution is characterized by a short supersonic region that is terminated by a relatively strong shock wave at $x = 11\%$. The outer nacelle-surface-pressure distribution shows only a tiny supersonic region. However, fairly large adverse pressure gradients downstream of the shock wave make the flow susceptible to separation above the pylon at the downstream end of the interference region. The gray shaded areas in Fig. 11 mark measured pressure-fluctuation amplitudes. Particularly, the pressure fluctuations at the outer nacelle surface downstream of $x \geq 6\%$ indicate shock-wave oscillations.

The observed fluctuations are nearly periodic. Considering the power spectral analysis in Fig. 12 of the pressure-based lift coefficient PSD(c_l) in the interference section, a peak at a reduced circular frequency of $k = 2.601$ is observed. At the same frequency, the fluctuation amplitudes in the reference section are more than 20 dB lower. For the given Mach-number/incidence combination, increasing the Reynolds number from $Re_\infty = 2.26 \times 10^6$ to 3.56×10^6 yields a reduction in the fluctuation amplitude of about 1.1 dB, as well as a very slight decrease in the reduced frequency to $k = 2.560$. During the present tests, a simple countermeasure is applied (and will be discussed subsequently) to avoid this kind of aerodynamic instability. The power spectral density in Fig. 12 shows that a reduction in the lift-fluctuation amplitudes of more than 15 dB could be achieved at these flow conditions. Figure 12 also shows the offwind ground-vibration test results (see Table 1) for reference. The present periodic unsteady airloads most likely excite the wing-torsion/nacelle-ovalization mode at a reduced frequency $k \approx 2.6$. However, the maximum oscillation amplitudes are smaller than

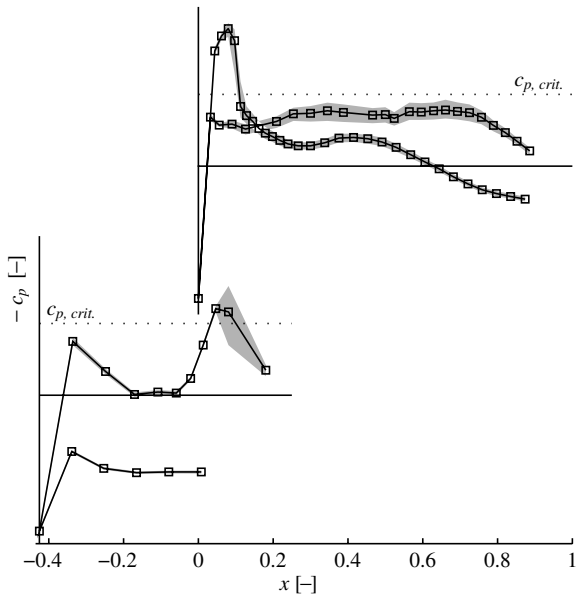

Fig. 11 Measured time-averaged $c_p(x)$ in the interference section; shaded areas indicate measured pressure fluctuations; $M_\infty = 0.755$, $Re_\infty = 2.26 \times 10^6$, $Su_0 = 0.359$, $\alpha = 0.53\,\text{deg}$, $\beta = 0\,\text{deg}$, and $\gamma = 0\,\text{deg}$.

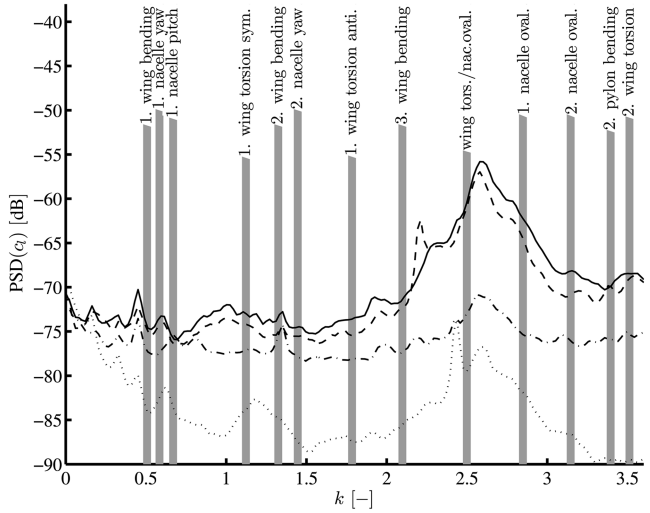

Fig. 12 Power spectral density (PSD) of the pressure-based lift coefficients PSD(c_l), and ground-vibration test results. Interference (solid line) and reference section (dotted line) at $Re_\infty = 2.26 \times 10^6$, interference section (dashed line) at $Re_\infty = 3.55 \times 10^6$, interference section (dashed-dotted line) at $Re_\infty = 2.27 \times 10^6$ with applied countermeasure; $M_\infty = 0.755 \pm 0.1\%$, $Su_0 = 0.358 \pm 1.1\%$, $\alpha = 0.55\,\text{deg} \pm 0.03\,\text{deg}$, $\beta = 0\,\text{deg}$, and $\gamma = 0\,\text{deg}$.

2 μm. Thus, the model may be considered rigid from an aerodynamic point of view. So the observed phenomenon is an aerodynamic instability rather than an aeroelastic instability.

Instantaneous velocity distributions are measured by PIV in a plane perpendicular to the pitching axis located close to the interference-section pressure taps. Figure 13 depicts the instantaneous streamwise development of mechanical energy $\mathbf{v} \cdot \nabla(\mathbf{v}^2/2)$ for the maximum downstream shock location at $M_\infty = 0.755$. This quantity clearly indicates shock- and expansion-wave locations. The top black area represents a part of the wing shape, the bottom black area corresponds to a part of the nacelle shape, and the white dotted-dashed line marks the shock front. Obviously, the adverse pressure gradient by the shock wave provokes a thickening of the wing pressure-side boundary layer such that the foot of the shock is spread to a lambda. Here, this is most likely linked to local shock-induced flow separation, which corresponds to numerical findings [6].

In conclusion, the observed pressure fluctuations in the interference region are caused by an aerodynamic instability. This aerodynamic instability includes shock-wave oscillations and, most likely, flow separation. The measured data qualitatively match observations based on numerical simulations [6]. All these findings indicate that a buffet-type mechanism causes the present instability in the wing–pylon–nacelle interference region.

The dependency of this instability on the Mach number and model incidence is investigated by systematically varying these parameters. The drag-fluctuation amplitude as an integral property is chosen to quantify the amount of instability, because the shock pulsations cause wave-drag oscillations. Figure 14 visualizes the dependency of the pressure-based drag-fluctuation amplitudes $\hat{c}_d$ in the interference section on Mach number M_∞ and incidence α. This figure is composed from more than 300 measured time series of data. The dark areas in the center represent a region of relatively high drag-fluctuation amplitudes ($\hat{c}_d > 3.5$ drag counts). The model incidence, which exhibits maximum fluctuation amplitudes, rises almost linearly with increasing Mach number. The corresponding maximum fluctuation amplitudes increase and then decrease with Mach number. Figure 14 also shows lines that correspond to main characteristics of the flowfield: interference-region sonic, wing-suction-side sonic, and nacelle-lift divergence. The aerodynamic instability occurs, of course, at interference-region supercritical Mach numbers. In 2-D flow, airfoil shock-buffet onset [21] typically occurs beyond lift-divergence Mach numbers, at which a local airfoil-lift maximum with respect to Mach number occurs at constant incidence. In contrast, the present aerodynamic instability occurs below nacelle-lift-divergence Mach numbers. This local nacelle-lift maximum at constant model incidence indicates that flow separation must already be present with respect to growing Mach numbers. The flow in the wing–pylon–nacelle interference region is inherently three-dimensional. Thus, buffet may occur locally even though the surrounding flow is still attached. Analogously, buffet onset at swept wings may appear at Mach numbers below wing-lift divergence [22,24,25]. Obviously, flow separation starts to occur close to the critical Mach number here. Nevertheless, it is interesting to note that the lines corresponding to the interference-region-sonic state, drag-fluctuation maximum, and nacelle-lift divergence are almost parallel in Fig. 14.

The local pressure-based drag-fluctuation amplitudes in the wing reference section are smaller than $\hat{c}_d \leq 1$. The Mach number at which the wing-pressure-side flow becomes locally supersonic is about $\Delta M_\infty = 0.06$ higher than in the interference region. The wing suction side gets sonic at the same inflow conditions as in the interference region. Accordingly, the wing-suction-side flow is only weakly affected by the wing–pylon–nacelle interference for moderate angles of attack, as is also indicated by the pressure distributions of Figs. 3 and 4.

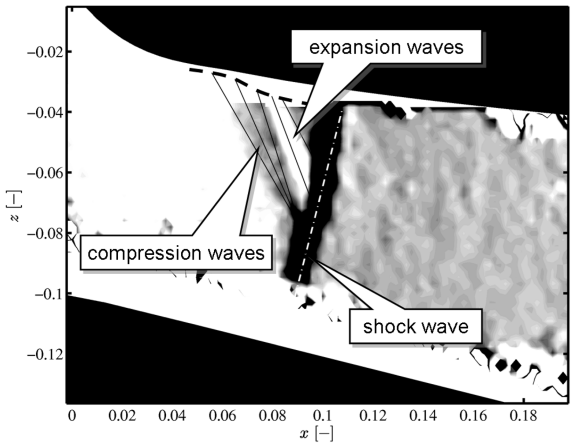

Fig. 13 PIV-evaluated streamwise development of mechanical energy $\mathbf{v} \cdot \nabla(\mathbf{v}^2/2)$ for the maximum downstream shock location; $M_\infty = 0.755$, $Re_\infty = 2.26 \times 10^6$, $Su_0 = 0.359$, $\alpha = 0.53\,\text{deg}$, $\beta = 0\,\text{deg}$, and $\gamma = 0\,\text{deg}$.

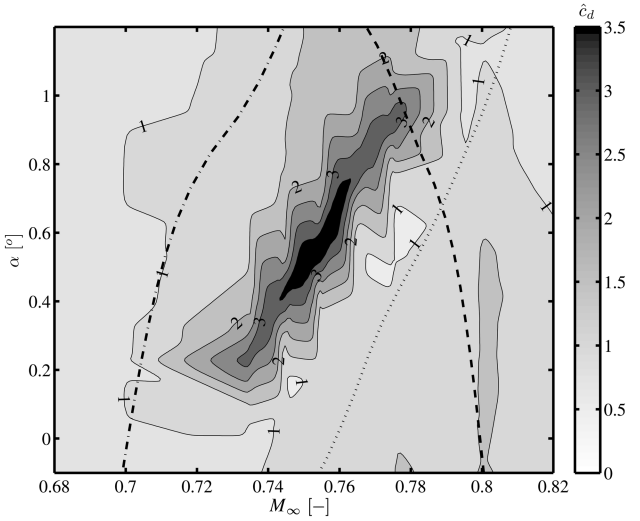

Fig. 14 Dependency of the pressure-based drag-fluctuation amplitudes $\hat{c}_d$ in the interference section on M_∞ and α; interference-region sonic (dashed-dotted line), wing-suction-side sonic (dashed line), and nacelle-lift divergence (dotted line) are indicated by lines; $Re_\infty = 2.23 \times 10^6 \pm 4.1\%$, $Su_0 = 0.359 \pm 1.5\%$, $\beta = 0\,\text{deg}$, and $\gamma = 0\,\text{deg}$; $\hat{c}_d$ denotes drag counts.

Getting back to the interference section, typical reduced buffet frequencies observed at supercritical airfoil flow [19,21,23] amount to $k = 0.4$–0.6. In the present case, Fig. 15 shows that the reduced frequencies based on wing–nacelle overlap the length amount to $k \approx 0.65$, which is a little higher than with 2-D airfoil flow. On a supercritical airfoil, the reduced suction-side buffet frequency decreases with increasing Mach number and with growing incidence [21]. Here, the model incidence, which exhibits maximum fluctuation amplitudes at constant Mach number, increases with increasing Mach number, and buffet occurs on the wing pressure side. Thus, one would expect monotonically increasing reduced frequencies. However, Fig. 15 shows a local minimum close to the global maximum fluctuation amplitude. Nevertheless, increasing the Reynolds number decreases the reduced frequency (see Fig. 15). This behavior matches observations at supercritical airfoils [21].

C. Aerodynamic Instability Countermeasure

The unsteady airloads induced by the previously described aerodynamic instability could be significantly reduced by a simple countermeasure. Figure 16 is a picture of the wing–pylon–nacelle interference region with this countermeasure, a small wire-mesh body, being installed between the wing and pylon. A proof-of-concept test for this flow control measure is performed during the present wind-tunnel test. However, the countermeasure is not varied, to minimize the cost-benefit ratio. Of course, there is an optimization potential. Unfortunately, its impact on the interference drag could not be measured here.

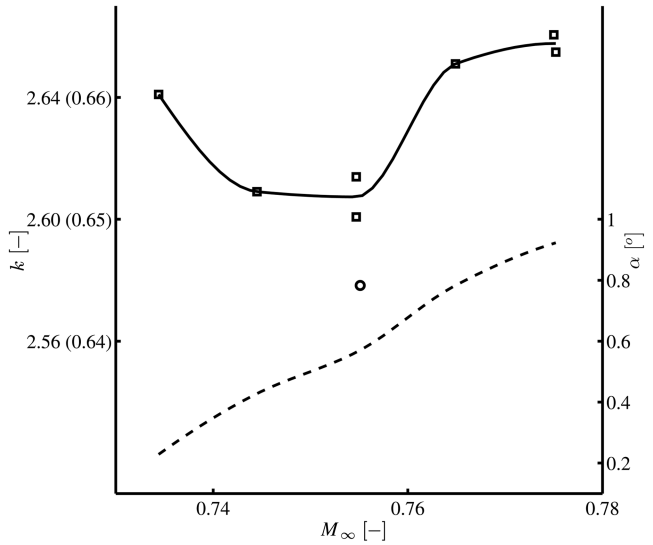

Fig. 15 Dependency of the maximum-amplitude reduced frequency k on M_∞ for $Re_\infty = 2.23 \times 10^6 \pm 4.1\%$ (squares and solid line) and for $Re_\infty = 3.54 \times 10^6$ (circles) with corresponding model incidence (dashed line); reduced frequencies k in parentheses are based on wing–nacelle overlap length; $Su_0 = 0.359 \pm 1.5\%$, $\beta = 0$ deg, and $\gamma = 0$ deg.

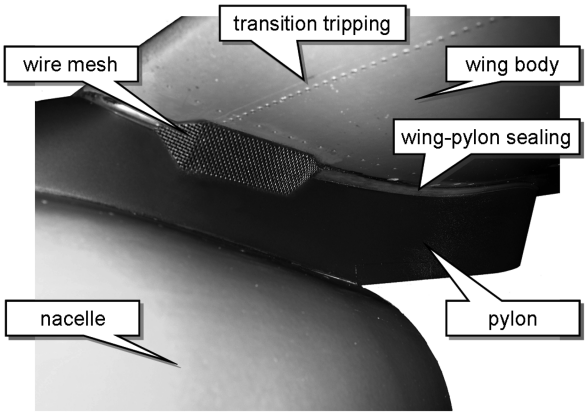

Fig. 16 Wing–pylon–nacelle interference region with applied wire-mesh countermeasure.

Figure 17 should be compared with Fig. 11. Figure 17 also shows typical time-averaged pressure distributions in the interference section, but with a wire-mesh body being installed. As intended, the supersonic region below the wing suction side and the pressure fluctuations above the nacelle outer side are reduced significantly by the countermeasure. Its operating principle is most likely based on two main features: First, the wire mesh acts as a displacement body such as a fixed shock-control bump [26,27]. Second, it works like D-strips [17] by allowing ventilation across the shock wave. The latter causes the boundary layer to act like a self-adaptive shock-control bump. A similar effect was most likely achieved by the inappropriate pylon–nacelle sealing in the pretest (see Fig. 4). Nevertheless, compared with a conventional bump, the present solution provides the advantage of self-adopting to the flow conditions in certain limits. However, a quantitative comparison between the present and a conventional solution is not performed here.

Figure 18 shows the pressure-based drag-fluctuation amplitudes $\hat{c}_d$ in the Mach-number/incidence plane as they are measured with an installed wire-mesh body. Compared with Fig. 14, the drag-oscillation amplitudes are reduced significantly. The interference-region-sonic line is shifted toward higher numbers by $\Delta M_\infty \geq 0.02$. Therefore, the interference drag will most likely also be reduced. Nevertheless, this conjecture has to be proven by future investigations. The interference-section lift-coefficient fluctuation is measured as being reduced by more than 75%, compared with the clean case. Unquestionably, the present data are obtained at a generic configuration and will not be representative for a specific 3-D design. However, for retrofit application, the potential advantages of the proposed countermeasure should be considered in comparison with conventional solutions.

IV. Conclusions

Results from recent experiments on unsteady wing–pylon–nacelle interference with tripped laminar-turbulent transition at transonic flow conditions were reported here. The tests were conducted in the Transonic Wind Tunnel, Göttingen (DNW-TWG) using an adaptive-wall test section and a newly designed model. The aerodynamic responses to forced model pitching, nacelle yawing, nacelle rolling,

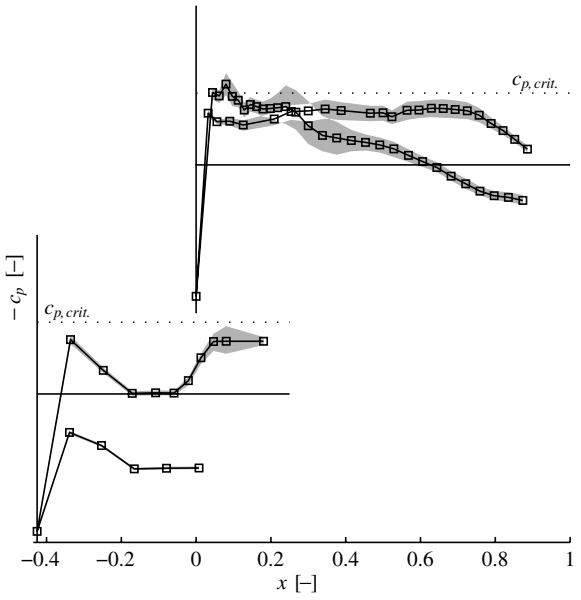

Fig. 17 Measured time-averaged $c_p(x)$ in the interference section with applied countermeasure. The gray shaded areas indicate the measured pressure fluctuations. $Ma_\infty = 0.755$, $Re_\infty = 2.27 \times 10^6$, $Su_0 = 0.361$, $\alpha = 0.54$ deg, $\beta = 0$ deg, and $\gamma = 0$ deg.

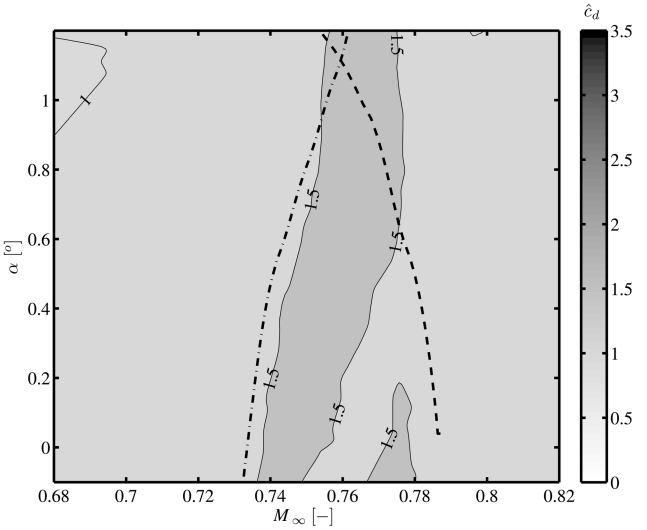

Fig. 18 Dependency of the $\hat{c}_d$ in the interference section on M_∞ and α with applied countermeasure; interference-region sonic (dashed-dotted line) and wing-suction-side sonic (dashed line) are indicated by lines; $Re_\infty = 2.24 \times 10^6 \pm 4.5\%$, $Su_0 = 0.361 \pm 1.6\%$, $\beta = 0\,\text{deg}$, and $\gamma = 0\,\text{deg}$.

model pitching plus nacelle yawing, and model pitching plus nacelle rolling were measured for sub- and supercritical Mach numbers. Tests with the rigid model were performed at flow conditions in which unsteady airloads occur.

The WIONA wind-tunnel model was designed to exhibit aerodynamic interference as observed in the wing–pylon–nacelle region of real aircraft. But the model shape was chosen to be as generic as possible to enable a detailed physical interpretation of the observed phenomena by reducing complexity. Both objectives were gained by a computational-fluid-dynamics-driven shape design of the model. Vice versa, the experimental data are used to improve and validate computational fluid dynamics codes.

The most significant results of the present investigation can be summarized as follows:

1) Linearization and superposition of model pitching, nacelle yawing, and nacelle rolling is possible, at least up to pitch-oscillation amplitudes $\hat{\alpha} \leq 0.14\,\text{deg}$, yawing amplitudes $\hat{\beta} \leq 0.44\,\text{deg}$, and rolling amplitudes $\hat{\gamma} \leq 2.5\,\text{deg}$, while taking the steady transonic flowfield into account.

2) A local buffet phenomenon in the wing–pylon–nacelle interference region may occur at Mach numbers that are only slightly higher than those at which the interference-region flow becomes locally supersonic.

3) A small wire-mesh body in the interference region is able to significantly reduce this local buffet and its corresponding unsteady airloads.

4) A leakage between the wing and the pylon fairing strongly affects the transonic wing–pylon–nacelle interference.

It can be concluded that the unsteady airloads of a wing/engine combination are strongly affected by interference effects when the flow in the wing–pylon–nacelle region locally becomes supersonic. Then it is necessary to account for the impact of the steady transonic flowfield on the unsteady airloads. However, linear superposition of the unsteady airloads due to specific motion modes is appropriate either without or at moderate flow separation. When the flow starts to separate locally, buffet might occur in the wing–pylon–nacelle interference region. Based on the present physical understanding, we intend to improve the numerical prediction capabilities of the observed phenomena.

Acknowledgments

The present investigation was performed within the ONERA and DLR, German Aerospace Center Common Transport Research Program (CTARP). The authors wish to thank R. Voß, J.-P. Grisval, and A. Soda for fruitful discussions and suggestions as well as D. Göge and M. Böswald for performing the structural identification. Thanks to Y. Amosse and F. Hervy for preparing and operating the model. Thanks also to J. Nuhn for thoroughly acquiring the data and to J. Berold and T. Büte for being responsible for the test setup. Finally, the authors would like to thank the staff of the Transonic Wind Tunnel, Göttingen (DNW-TWG) for their cooperation. Special thanks to J. Sperlich for proofreading the text.

References

[1] Försching, H., and von Diest, K., "Flutter Stability of Annular Wings in Incompressible Flow," *Journal of Fluids and Structures*, Vol. 5, No. 1, 1991, pp. 47–67. doi:10.1016/0889-9746(91)80011-2

[2] Hoheisel, H., "Aerodynamic Aspects of Engine-Aircraft Integration of Transport Aircraft," *Aerospace Science and Technology*, Vol. 1, No. 7, 1997, pp. 475–487. doi:10.1016/S1270-9638(97)90009-2

[3] Rudnik, R., Rossow C.-C., and Freiherr von Geyr, H., "Numerical Simulation of Engine/Airframe Integration for High-Bypass Engines," *Aerospace Science and Technology*, Vol. 6, No. 1, 2002, pp. 31–42. doi:10.1016/S1270-9638(01)01139-7

[4] Zingel, H., "Measurements of Steady and Unsteady Airloads on a Stiffness Scaled Model of Modern Transport Aircraft Wing," International Forum on Aeroelasticity and Structural Dynamics, Germany, Deutsche Gesellschaft für Luft- und Raumfahrt Paper 91-06, 1991.

[5] Triebstein, H., Schewe, G., Zingel, H., and Vogel, S., "Measurement of Unsteady Airloads on an Oscillating Engine and a Wing/Engine Combination," *Journal of Aircraft*, Vol. 31, No. 1, 1994, pp. 97–102.

[6] Soda, A., "Numerical Investigation of Unsteady Transonic Shock/Boundary-layer Interaction for Aeronautical Application," Dr.-Ing. Dissertation, RWTH Aachen Univ., Aachen, Germany, 2006; also Deutsches Zentrum für Luft- und Raumfahrt, Forschungsbericht Paper 2007-03, 2007.

[7] Wedemeyer, E., Taylor, N. J., and Holst, H., "Adaptive Wall Techniques," *Wind Tunnel Wall Correction*, AGARD Rept. AG 336, Neuilly-sur-Seine, France, 1998.

[8] Cebeci, T., and Bradshaw, P., *Momentum Transfer in Boundary Layers*, McGraw–Hill, New York, 1979.

[9] Voß, R., "Wall Correction Methods for Dynamic Tests," *Wind Tunnel Wall Correction*, AGARD Rept. AG 336, Neuilly-sur-Seine, France, 1998.

[10] Richter, K., and Rosemann, H., "Experimental Investigations of Trailing-Edge Devices at Transonic Speeds," *The Aeronautical Journal*, Vol. 106, No. 1058, 2002, pp. 185–193.

[11] Soda, A., and Tefy, T., "Numerical Investigation of Wing–Nacelle Interference Effects at Transonic Flow Conditions for a Generic Transport Aircraft Configuration," *New Results in Numerical and Experimental Fluid Mechanics*, edited by C. Breitsamter, B. Laschka, H.-J. Heinemann, and R. Hilbig, Springer, Berlin, Vol. 4, 2004, pp. 82–90.

[12] Rossow, C.-C., Godard, J.-L., Hoheisel, H., and Schmitt, V., "Investigations of Propulsion Integration Interference Effects on a Transport Aircraft Configuration," *Journal of Aircraft*, Vol. 31, No. 5, 1994, pp. 1022–1030.

[13] Schewe, G., "Force Measurements in Aeroelasticity Using Piezo-electric Multicomponent Transducers," International Forum on Aeroelasticity and Structural Dynamics, Germany, DGLR Paper 91-06, 1991.

[14] Kompenhans, J., Schröder, A., Engler, R., Klinge, F., and Stasicki, B., ""Development and Application of Image Based Measurement Techniques for Aerodynamic Investigations in Wind Tunnels," *International Scientific Conference High-Speed Flow Fundamental Problems*, TsAGI, Moscow, 2004.

[15] Klein, C., Engler, R., Sachs, W., and Henne, U., "Application of Pressure Sensitive Paint (PSP) for Determination of the Pressure Field and Calculation of Forces and Moments of Models in a Wind Tunnel," *Experiments in Fluids*, Vol. 39, No. 2, 2005, pp. 475–483. doi:10.1007/s00348-005-1010-8

[16] Göge, D., and Böswald, M., "Structural Dynamic Test on WIONA II," Deutsches Zentrum für Luft- und Raumfahrt, Interner Bericht Paper 232-2005 C08, 2005.

[17] Dietz, G., "Passive Shock Control Concept for Drag Reduction in Transonic Flow," *Journal of Aircraft*, Vol. 42, No. 3, 2005, pp. 794–798. doi:10.2514/1.11881

[18] Dietz, G., Schewe, G., Kießling, F., and Sinapius, M., "Limit-Cycle-Oscillation Experiments at a Transport Aircraft Wing Model," *Proceedings of the International Forum on Aeroelasticity and Structural Dynamics*, Confederation of European Aerospace Societies, 2003.

[19] Dietz, G., Schewe, G., and Mai, H., "Experiments on Heave/Pitch Limit-Cycle Oscillations of a Supercritical Airfoil Close to the Transonic Dip," *Journal of Fluids and Structures*, Vol. 19, No. 1, 2004, pp. 1–16. doi:10.1016/j.jfluidstructs.2003.07.019

[20] Dietz, G., Schewe, G., and Mai, H., "Amplification and Amplitude Limitation of Heave/Pitch Limit-Cycle-Oscillations Close to the Transonic Dip," *Journal of Fluids and Structures*, Vol. 22, No. 4, 2006, pp. 505–527. doi:10.1016/j.jfluidstructs.2006.01.004

[21] Stanewsky, E., and Basler, D., "Experimental Investigation of Buffet Onset and Penetration on a Supercritical Airfoil at Transonic Speeds," *Aircraft Dynamic Loads Due to Flow Separation*, CP-483, AGARD, Neuilly-sur-Seine, France, 1990.

[22] Caruana, D., Mignosi, A., Corrège, M., Pourhiet, A., and Rodde, A. M., "Buffet and Buffeting Control in Transonic Flow," *Aerospace Science and Technology*, Vol. 9, No. 7, 2005, pp. 605–616. doi:10.1016/j.ast.2004.12.005

[23] Brunet, V., Deck, S., Jacquin, L., and Molton, P., "Transonic Buffet Investigations Using Experimental and DES Techniques," *7th ONERA-DLR Aerospace Symposium (ODAS 2006)*, ONERA, Châtillon, France, 2006, pp. 1–7.

[24] Gadeberg, B. L., and Ziff, H. L., "Flight-Determined Buffet Boundaries of Ten Airplanes and Comparisons with Five Buffeting Criteria," NACA Rept. RM A50I27, 1951.

[25] Elsenaar, A., "Separation in Transonic Flow: A Shocking Experience," National Aerospace Laboratory, Rept. TP 97151, Amsterdam, The Netherlands, 1997.

[26] Stanewsky, E., Délery, J., Fulkner, J., and Geißler, W., "Synopsis of the Project EUROSHOCK II," *Drag Reduction by Shock and Boundary Layer Control*, Notes on Numerical Fluid Mechanics and Multidisciplinary Design, Vol. 80, Springer, Berlin, 2002, pp. 1–124.

[27] Holden, H. A., and Babinsky, H., "Shock/Boundary Layer Interaction Control Using 3-D Bumps," *Proceedings of the CEAS Aerospace Aerodynamics Research Conference*, Confederation of European Aerospace Societies, 2002.